Science Advances
AAAS

advances.sciencemag.org/cgi/content/full/4/7/eaat5168/DC1

Supplementary Materials for

Engineering stable interfaces for three-dimensional lithium metal anodes

Jin Xie, Jiangyan Wang, Hye Ryoung Lee, Kai Yan, Yuzhang Li, Feifei Shi, William Huang, Allen Pei, Gilbert Chen, Ram Subbaraman, Jake Christensen, Yi Cui*

*Corresponding author. Email: yicui@stanford.edu

Published 27 July 2018, *Sci. Adv.* **4**, eaat5168 (2018)
DOI: 10.1126/sciadv.aat5168

This PDF file includes:

Etching of C/SiO_2 nanoparticles in HF solution

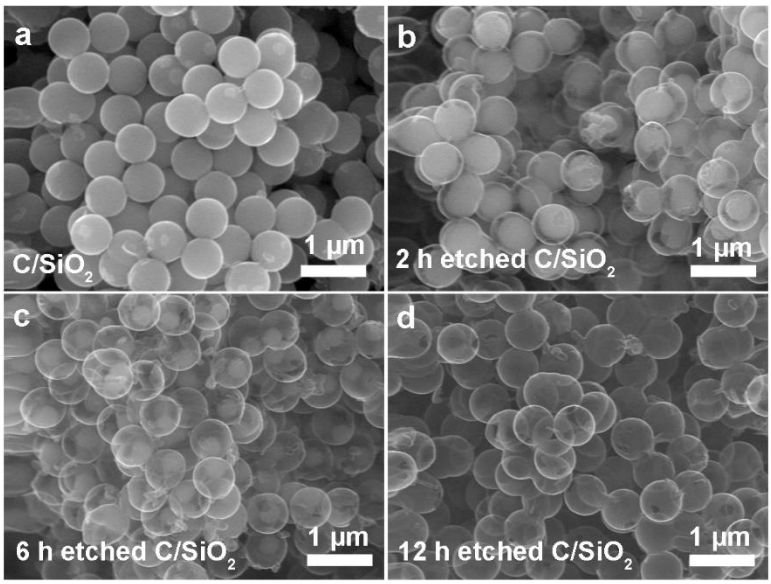

Fig. S1. Etching of C/SiO_2 nanoparticles in HF solution. (**a**) SEM characterization of C/SiO_2 nanoparticles prior to HF etching. (**b**) SEM characterization of C/SiO_2 nanoparticles after etching in HF solution for 2 hours. (**c**) SEM characterization of C/SiO_2 nanoparticles after etching in HF solution for 6 hours. (**d**) SEM characterization of C/SiO_2 nanoparticles after etching in HF solution for 12 hours.

To remove the templates, the SiO_2 nanoparticles were soaked in 10% HF solution. Although the reported etching rates of SiO_2 is fast in HF solution (*38, 39*); SiO_2 cores remained visible inside the carbon shells after 2 hours of etching (fig. S1b) and 6 hours of etching (fig. S1c), respectively. Nevertheless, SiO_2 cores in carbon shells can be completely removed after soaking in HF solution for a long period of 12 hours (fig. S1d), which suggested HF can indeed slowly penetrate through carbon shells and etch away SiO_2 cores. The etching result, together with the electrolyte drying result presented in Fig. 3 of the main text, highlighted the as synthesized carbon shell prepared by carbonization of RF resin shell is only capable of slowing down electrolyte penetrating, but cannot shut it down completely. In fact, the existence of micropores has been reported for various carbon materials prepared by the carbonization of RF resins (*28-30*). More specifically, Li et al. reported the HCS prepared by carbonization of RF resin has two most dominated pore-size distribution peaks at 0.5-0.6 and 1.3-1.5 nm (*29*). These micropores served as a double-edged sword. One the one hand, without them, SiO_2 cores cannot be removed. On the other hand, they also allowed electrolyte penetration, which will react with lithium to reduce the battery cycle

stability. Therefore, these pores need to be sealed after etching. With ALD coating, we have shown in Fig. 3 of the main text that electrolyte cannot penetrate inside.

Top-view SEM characterization of HCS electrode and ALD Al_2O_3/HCS electrode after electrochemical lithium plating

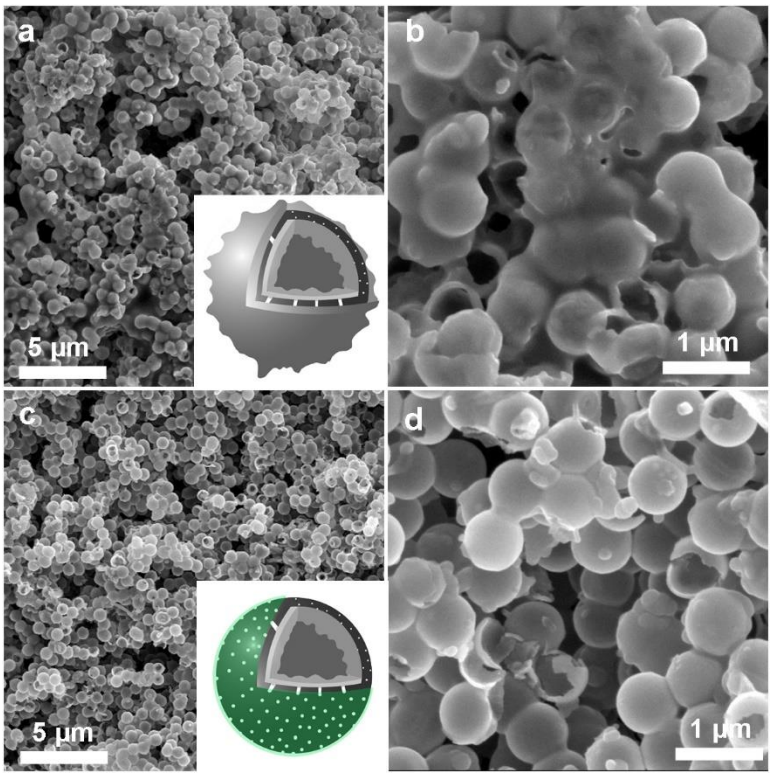

Fig. S2. Top-view SEM characterization of HCS electrode and ALD Al_2O_3 HCS electrode after initial electrochemical lithium plating. (**a** and **b**) Top view SEM images of HCS electrode after electrochemical lithium plating. Inset shows the schematic. (**c** and **d**) Top view SEM images of ALD Al_2O_3 HCS electrode after electrochemical lithium plating. Inset shows the schematic.

Figure S2 presents typical SEM images of HCS electrode and ALD Al_2O_3 HCS electrode after initial electrochemical lithium plating. Without ALD coating, lithium deposited on top of HCS (fig. S2a and S2b). Together with FIB/SEM characterization in Fig. 3 of the main text, we can conclude that lithium deposited both inside and outside HCS. For comparison, the surface of ALD Al_2O_3/HCS electrode was relatively clean after lithium plating. Together with FIB/SEM characterization in Fig. 3 of the main text, we can conclude that lithium deposited inside HCS.

XPS characterization of pristine Cu, ALD Al_2O_3 coated Cu and ALD Al_2O_3 coated HCS/Cu after removal of HCS

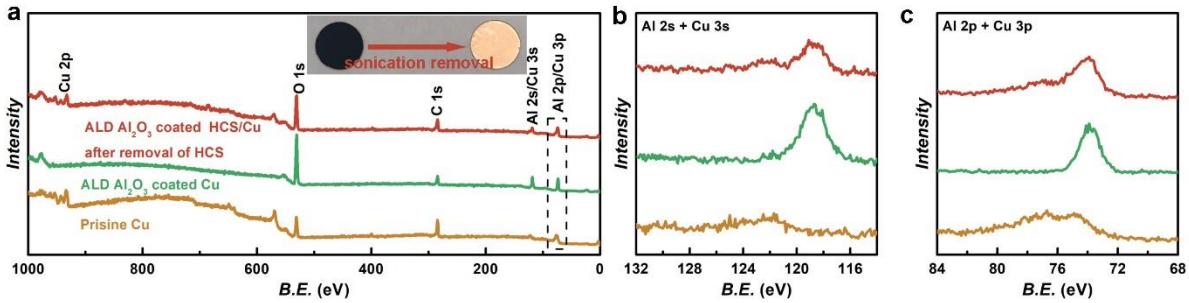

Fig. S3. XPS characterization. (**a**) XPS survey scans of pristine Cu, ALD Al_2O_3 coated Cu and ALD Al_2O_3 coated HCS/Cu after removal of HCS. Inset shows optical images of ALD Al_2O_3 coated HCS/Cu electrode before and after removal of Al_2O_3/HCS. (**b**) XPS fine scans of pristine Cu, ALD Al_2O_3 coated Cu and ALD Al_2O_3 coated HCS/Cu after removal of HCS in the 114-132 eV binding energy region. (**c**) XPS fine scans of pristine Cu, ALD Al_2O_3 coated Cu and ALD Al_2O_3 coated HCS/Cu after removal of HCS in the 68-84 eV binding energy region.

XPS analysis was performed to test if the Cu surface has been covered with Al_2O_3 after ALD coating. After ALD Al_2O_3 coating on HCS/Cu electrode, we sonicated the electrode vigorously to remove ALD Al_2O_3 coated HCS on the Cu current collector. We then performed XPS to analyze the surface chemical composition of the obtained Cu current collector (referred to as "ALD Al_2O_3 on HCS/Cu after removal of HCS"), along with pristine Cu and ALD Al_2O_3 coated pristine Cu (referred to as "ALD Al_2O_3 on Cu"). As shown in the XPS survey scans (fig. S3), the surface of Cu after coating of ALD Al_2O_3 and the removal of HCS shown strong Al signals, compared to pristine Cu. As Al and Cu peaks often overlapped (Al 2p and Cu 3p; Al 2s and Cu 3s), we further provided fine scans in 114-132 eV region (fig. S3b) for Al 2s and Cu 3s peaks, and fine scans in 68-84 eV region (fig. S3c) for Al 2p and Cu 3p, respectively. The XPs analysis clearly showed that the Cu substrate underneath dense HCS packing was covered by Al_2O_3.

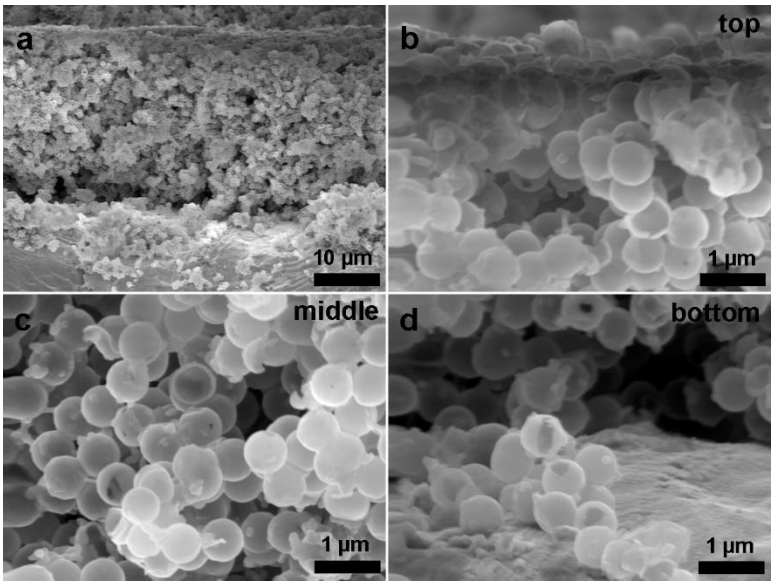

Fig. S4. Cross-sectional SEM characterization of ALD Al_2O_3/HCS electrode after lithium plating. (**a**) SEM image of entire cross-section of ALD Al_2O_3/HCS electrode after lithium plating. (**b** to **d**) Zoomed in SEM images of top, middle and bottom of ALD Al_2O_3/HCS electrode after lithium plating.

SEM characterization was performed to acquire cross-sectional images of lithium plated ALD Al_2O_3/Cu electrodes. ALD Al_2O_3/HCS electrodes after lithium plating were torn in half to acquire cross-sectional views (fig. S4). Compared to FIB/SEM images presented in the main text, the ALD Al_2O_3/HCS electrodes torn apart allowed to examine the whole electrode at a large scale. No obvious lithium dendrites were observed growing outside of ALD Al_2O_3 coated HCS in low magnification SEM images (fig. S4a) and high magnification near the bottom of the electrode (fig. S4b-S4d).

Optical and SEM images of ALD Al_2O_3/HCS electrodes after different amount of electrochemical lithium plating

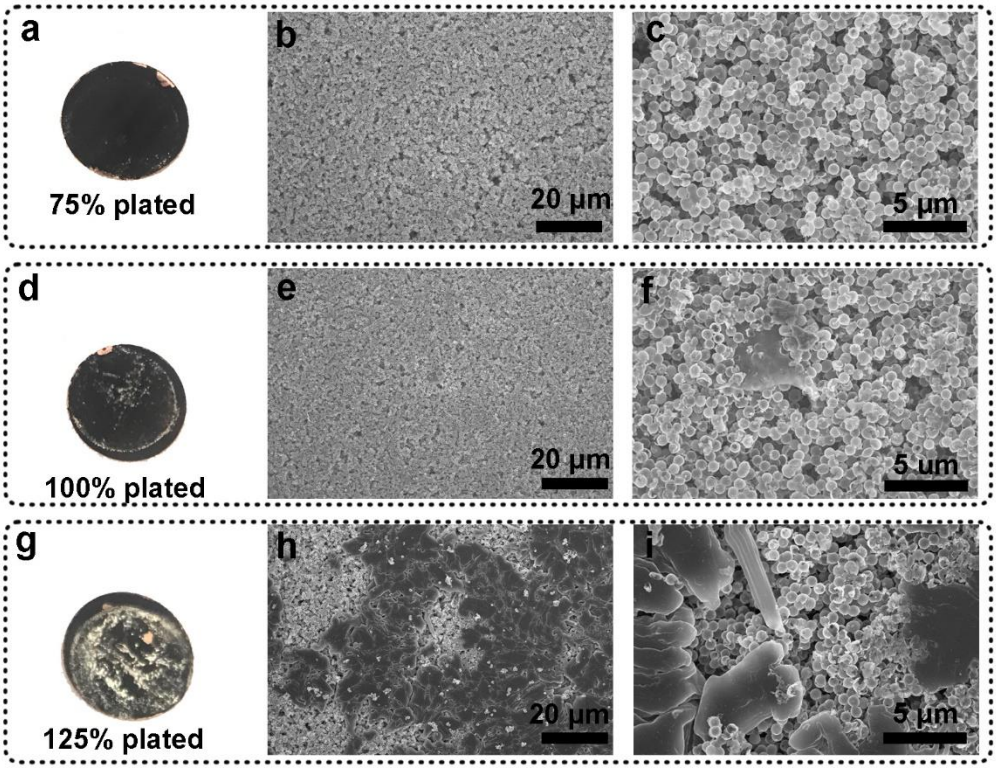

Fig. S5. Optical and SEM images of ALD Al_2O_3/HCS electrodes after different amounts of electrochemical lithium plating. (**a** to **c**) Optical images and SEM images of ALD Al_2O_3/HCS electrodes after 75% theoretical capacity lithium plating. (**d** to **f**) Optical images and SEM images of ALD Al_2O_3/HCS electrodes after 100% theoretical capacity lithium plating. (**g** to **i**) Optical images and SEM images of ALD Al_2O_3/HCS electrodes after 125% theoretical capacity lithium plating. The areal loading of HCS is 0.5mg/cm^2.

The theoretical areal capacity of ALD Al_2O_3/HCS electrodes is a function of areal loading of HCS, pore size of HCS and shell thickness of HCS. The theoretical areal capacity can be calculated according to the following equations:

(E1) Lithium capacity of individual HCS: $(\pi d^3/6)\rho_{Li}/M_{Li}\times 96485/3.6$

(E2) Weight of individual HCS: $(\pi D^3/6-\pi d^3/6)\times\rho_C$

(E3) Specific capacity: $(96485\times d^3\times\rho_{Li})/(3.6\times(D^3-d^3)\times\rho_C\times M_{Li})$

D is the outside diameter of HCS, d is the inside diameter of HCS, ρ_{Li} is the density of lithium, ρ_C is the density of carbon and M_{Li} is the atomic weight of lithium. For a HCS with a 685 nm outside diameter and 645 nm inside diameter, the theoretical capacity is close to 5,200 mAh/g_C.

However, in reality, when plating capacity reaches 100% of theoretical capacity, not all lithium can be confined inside HCS. Optical images and top view SEM images are provided for ALD Al_2O_3/HCS electrodes with different amounts of electrochemically plated lithium (fig. S5). If the plated amount of lithium exceeded more than 100% of the theoretical capacity, lithium would plate outside of HCS. Large agglomerate of lithium with size of several micrometers can be seen in the SEM images (fig. S5h and S5i). Correspondingly, shiny metallic color was observed in the optical image (fig. S5g). For comparison, no exposed lithium was observed in the top view SEM images (fig. S5b and S5c) and the electrode remained completely dark in the optical image (fig. S5a) for electrode with 75% theoretical capacity of lithium plated. For electrodes plated with exactly 100% theoretical capacity, small amount of exposed lithium was observed (fig. S5d-S5f), which might be due to the slightly non-uniformity of HCS loading and/or current distribution. The areal capacity of HCS electrodes is therefore a function of pore size of HCS, shell thickness of HCS and areal loading of HCS. The result indicates majority of lithium could be confined in the HCS if the lithium plating capacity is kept below 75% of the theoretical capacity. Small percentage of broken HCS during synthesis, slightly non-uniform distribution of HCS across the electrode area and/or slightly non-uniform ALD coating may be factors for lithium start to plate outside when the lithium plating capacity reaches 100% of theoretical capacity.

Cycle performance in carbonate electrolyte with and without additives

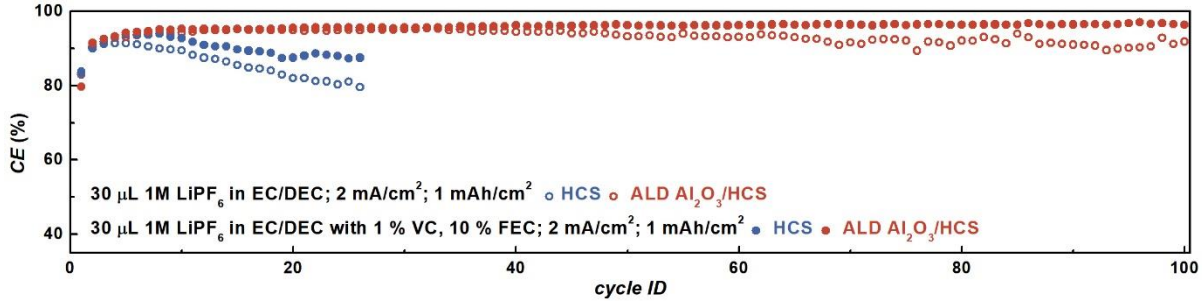

Fig. S6. Cycle performance in carbonate electrolyte with and without additives. Coulombic efficiency versus cycle number plots of HCS and ALD Al_2O_3/HCS in 30μL 1M $LiPF_6$ EC/DEC electrolyte with and without VC/FEC additives.

Cycling tests were also performed in additive-free EC/DEC electrolyte (fig. S6). For ALD Al_2O_3/HCS electrodes, the coulombic efficiency was similar in electrolytes with and without VC/FEC additives. However, the coulombic efficiency started to fluctuate slightly in late cycles in additive-free electrolyte, possibly due to electrolyte depletion caused by parasitic reactions in the counter electrode. In comparison, the coulombic efficiency of HCS electrodes in additive-free electrolyte was lower than that in electrolyte with VC/FEC additives. The results confirmed that electrolyte additives could improve cycle coulombic efficiency if lithium metal is not protected well.

Cycle performance of symmetric cells

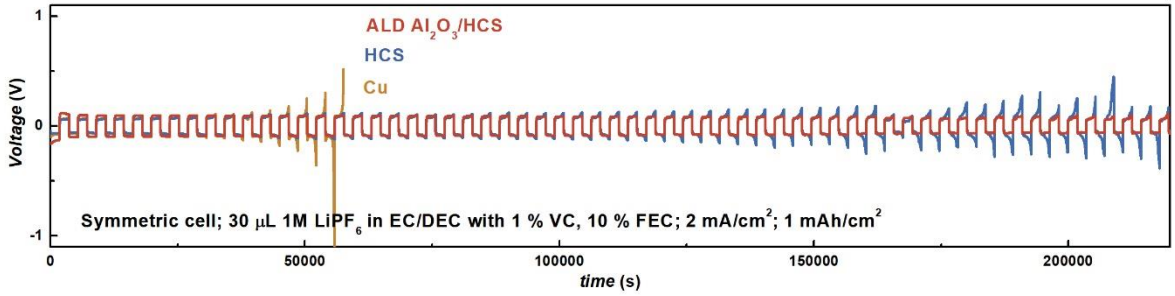

Fig. S7. Cycle performance of symmetric cells. Voltage versus time plots of Cu, HCS and ALD Al_2O_3/HCS symmetric cells in 30μL 1M $LiPF_6$ EC/DEC electrolyte with 1% VC and 10% FEC.

While the half-cell geometry provides coulombic efficiency information, symmetric cell provides rich information in battery cycle life. To understand the failure mechanism in more detail, we performed rigorous symmetric cell testing with a limited amount of Li and limited amount of electrolyte to mimic realistic cycling conditions. Briefly, a controlled amount of 4 mAh/cm^2 of lithium was plated onto Cu, HCS, and ALD Al_2O_3/HCS electrodes in a half-cell geometry. Electrodes were then extracted by disassembling half-cells. In a symmetric cell geometry, two pieces of lithium plated electrodes were used as both working and counter electrodes. 30 μL of electrolyte was added as the same as half-cell geometry. In this design, as both the amount of active lithium and amount of electrolyte are limited, cells with more parasitic reactions are more prone to fail as either active lithium or electrolyte can be depleted. The result reflects the effectiveness of ALD Al_2O_3/HCS in minimizing parasitic reactions and extending lithium metal cycle life.

Cycle performance in ether electrolyte

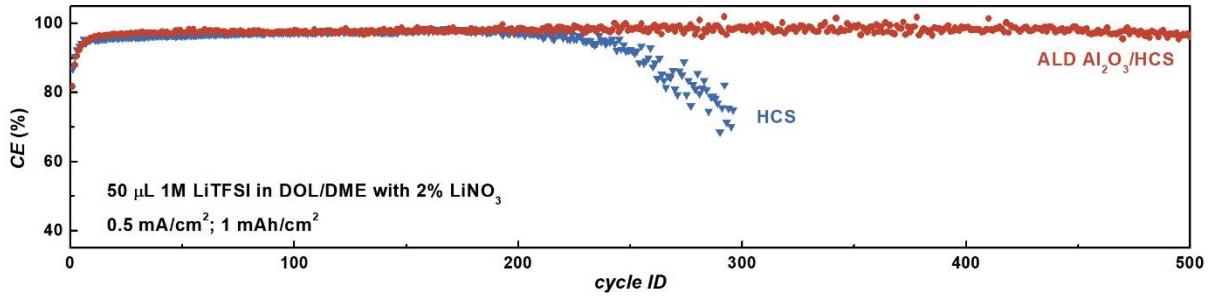

Fig. S8. Cycle performance in ether electrolyte. Coulombic efficiency versus cycle number plots of HCS and ALD Al_2O_3/HCS cells in 50μL 1:1 DOL/DME electrolyte with 1 M LiTFSI and 2% $LiNO_3$.

The addition of $LiNO_3$ additive could slow down the consumption of electrolyte at the counter electrode and therefore allow us to investigate the stability (e.g. coulombic efficiency and cycle life) of the working electrode more carefully. Cycling tests at lower $LiNO_3$ concentration were also performed in fig. S8.

STEM-EDX line scan of ALD AlF_3–coated HCS

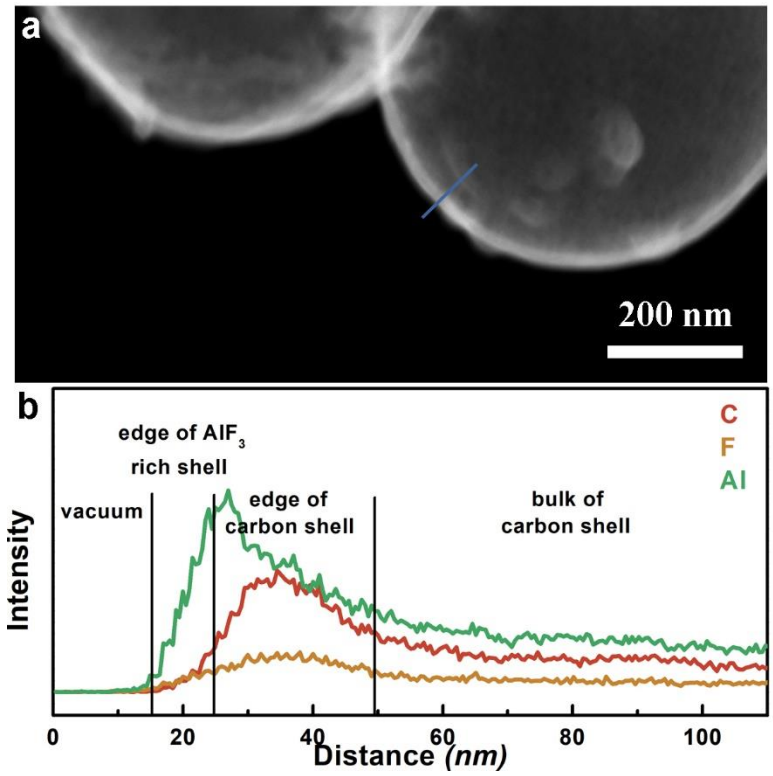

Fig. S9. STEM-EDX line scan of ALD AlF_3–coated HCS. (**a**) STEM image and (**b**) EDX line scan of ALD AlF_3/HCS.

AlF_3 has also been investigated as a coating layer on HCS and exhibited core-shell structures confirmed by STEM-EDX (fig. S9). The AlF_3 coating was applied using ALD as well. The precursors used to coat AlF_3 in this study are TiF_4 as the F source and $AlCl_3$ as the Al source (*26*).

Additional cycle performance data of ALD Al_2O_3/HCS and ALD AlF_3/HCS electrodes

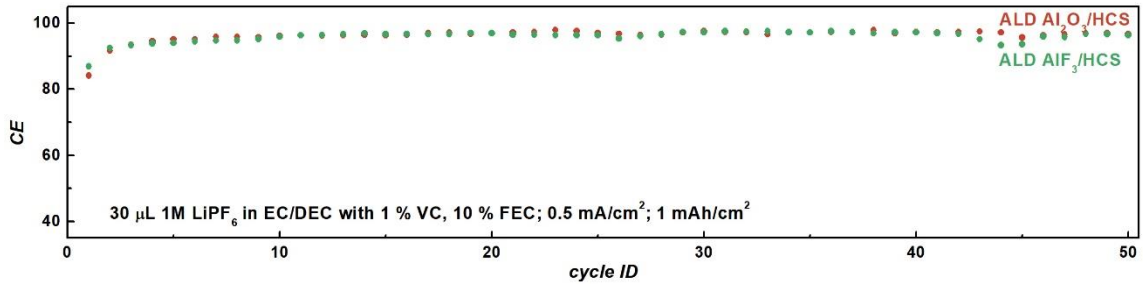

Fig. S10. Additional cycle performance data of ALD Al_2O_3/HCS and ALD AlF_3/HCS electrodes. Coulombic efficiency versus cycle number plots of ALD Al_2O_3/HCS and ALD AlF_3/HCS in 30μL EC/DEC electrolyte with 1M $LiPF_6$, 1% VC and 10% FEC.

In addition to Al_2O_3, AlF_3 layer was also prepared using ALD on HCS as a proof-of-concept. Similar performance has been observed for ALD Al_2O_3/HCS electrode and ALD AlF_3/HCS electrode in the carbonate electrolyte (fig. S10).